DOI: 10.15480/882.9308

Eighth International Symposium on Marine Propulsors
smp'24, Berlin, Germany, March 2024

A Normal Numerical Prediction Method for Cavitation Erosion Risk of Marine propeller

Zheng En-hui[1,2]; Cao Yan-tao[1,2]; Xu Liang-hao[1,2]; Peng Xiao-xing[1,2]

[1]National Key Laboratory on Ship Vibration & Noise, China Ship Scientific Research Center, Wuxi, 214082, China
[2]Taihu Laboratory of Deepsea Technological Science, Wuxi, 214082, China

ABSTRACT

With the increase of ship speeds and tonnages, and the need for improved propulsion efficiency, the occurrence of cavitation is becoming a more common phenomenon in ships. However, accurately predicting the risk of cavitation erosion remains a huge challenge due to its complexity. Based on the existing hydrodynamic mechanism, this paper attempts to develop a normal numerical method to predict the risk of cavitation erosion on marine propellers. First, the fluctuating pressure change rate at the ship's bottom plate between the minimum and maximum fluctuating pressure over one period is used to qualitatively assess the intensity of cavitation bubble collapse. By comparing numerical predictions with experimental and actual results, fluctuating pressure change rate exceeding 1.2×10^6 is established as the threshold for determining the presence of cavitation erosion risk. Second, when the local pressure and potential energy change rate on the propeller surface both are greater than 10% of the maximum pressure change rate and potential energy change rate over several cycles, the process is considered to have the potential to induce cavitation erosion risk. After meeting these conditions, the integration of potential energy change rates on the blade over several cycles reveals the distribution and intensity of cavitation erosion risk. This numerical prediction method for cavitation erosion risk was applied to five propellers. The numerical prediction results agree well with experimental results obtained through paint tests and actual cavitation erosion results. This validation confirms its engineering practicality.

Keywords

Cavitation erosion risk, Numerical prediction method, Marine propeller

1 INTRODUCTION

In engineering, considering the propulsion efficiency, it is often challenging to avoid cavitation. But the occurrence of cavitation does not necessarily lead to cavitation erosion. To ensure propulsion efficiency while avoiding the impact of cavitation erosion, propeller design needs to strike a delicate balance between cavitation and cavitation erosion. This necessitates a reliable and effective method for predicting cavitation erosion risk, which serves as a basis for propeller design.

the occurrence of cavitation erosion is due to the immense pulse pressure generated by cavitation collapse or the high-speed micro-jets impact the material surface(Pan et al 2004). Over time, this accumulation of forces leads to material fatigue and damage. This explanation highlights that cavitation encompasses two aspects: first, the hydrodynamic mechanisms of cavitation, which can be simplistically described as the loads exerted by the cavitation flow field on material surfaces, and second, how these loads lead to material damage. The term "cavitation erosion risk prediction" focuses solely on the assessment of the impact dynamics of cavitation flow fields on solid surfaces and does not address the mechanical properties of the materials involved.

Cavitation erosion risk prediction methods mainly include experimental and numerical approaches. In the field of engineering applications, paint test method is typically used to predict cavitation erosion risk on propellers. The paint test involves applying soft material to model surfaces and subjecting the model to a cavitation environment for several hours. The condition of the material's delamination is then used to assess cavitation erosion risk. This provides a basis for the design of hydraulic machinery like propellers. Cao et al. (2017) used paint test method to assess cavitation erosion risk areas for a three-dimensional twisted NACA0009 hydrofoil under two different conditions. Li et al.(2012) conducted paint test method for NACA0015 hydrofoils at an 8-degree attack angle of and NACA0018-45 hydrofoils at a 6.5-degree attack angle in cavitation conditions. This article will also use the results of paint test to validate the accuracy of numerical predictions.

In recent years, numerical methods have been rapidly advancing, and an increasing number of researchers have been attempting to use numerical methods to predict cavitation erosion risk. In practice, cavitation bubble collapse occurs at a very small scale (on the order of micrometers and microseconds). This makes it exceedingly difficult for numerical simulations to capture the cavitation bubble collapse process accurately, and it is even more challenging to extend these simulations to

model-scale or full-scale. Therefore, current numerical predictions of cavitation erosion risk still rely on qualitative assessments using macroscopic flow field properties.

Researchers have developed various numerical methods for predicting cavitation erosion risk, relying on characteristic parameters of the cavitation flow field such as pressure, vapor volume fraction, and potential energy. Dular et al. (2006) associated the standard deviation of vapor volume fraction with cavitation erosion risk. Nohmi et al. (2008) defined a set of simple functions of wall pressure and vapor volume fraction to measure cavitation erosion risk. Li et al. (2012) proposed a cavitation erosion risk characterization parameter based on the pressure time derivative. They determined a fixed threshold for the rate of pressure change by comparing it with paint test results. Leclercq et al. (2016) introduced an energy transfer mechanism for shockwaves generated by bubble collapse, based on potential energy assumptions. This model combines local potential energy rate changes with a solid angle model. Patella et al. (2012) assumed that the initial potential energy of the bubble structure is first converted into kinetic energy at the bubble surface. As the bubble's volume decreases, the kinetic energy gradually focuses towards the bubble's center. When cavitation collapse, all the energy is released to the surface. Melissaris et al. (2020), building upon Leclercq's work, considered the pressure change rate as a small quantity within potential energy rate changes, they used only the vapor volume fraction change rate term to predict cavitation erosion risk and employed a method to filter out regions with low energy radiation by highlighting extreme values.

The above-mentioned cavitation erosion risk prediction methods can yield results similar to model experiments within a certain range. However, they still face challenges, primarily in two aspects: First, a universal indicator that can accurately determine the presence of cavitation erosion risk under different operating conditions and models has not yet been identified. Second, the correspondence between numerical predictions of cavitation erosion risk and paint test results or full-scale ship results is not very accurate.

Based on the characteristics of cavitation erosion mechanisms and numerical simulation methods, this article proposes a cavitation erosion risk prediction method. Regarding the first aspect, according to the cavitation bubble collapse mechanism, when the environmental pressure increases rapidly, it accelerates bubble collapse. Since current numerical simulation methods cannot accurately capture the significant impact loads, this article qualitatively assumes that when the environmental pressure increase rate is sufficiently high, it can lead to cavitation erosion risk. Concerning the second aspect, this article simultaneously uses parameters such as pressure change rate and potential energy change rate on the propeller surface to predict cavitation erosion risk. A percentage threshold determination method is used to filter out processes with low bubble collapse degrees, which remains applicable under different computational conditions. Finally, by integrating potential energy rate change on the blade surface that meets the selection criteria, the absorbed energy on the wall over a period can be obtained. The distribution of absorbed wall energy can reveal the areas and intensity of cavitation erosion risk.

Using the methods described above, this study conducted numerical predictions of cavitation erosion risk for five sets of propeller models. The numerical results exhibited a high level of consistency when compared to the results of paint test method and actual propeller cavitation erosion results. This validation confirms the practical utility of the cavitation erosion risk numerical prediction method proposed in this article.

2 CAVITATION EROSION RISK NUMERICAL PREDICTION METHOD

2.1 Presence of Cavitation Erosion Risk Determination Method

Based on the erosive characteristics caused by the impact loads from cavitation bubble collapse, cavitation erosion areas are often found near the trailing edge of blades, where cloud clusters occur. In these regions, the cavitation bubbles are extremely small in scale, and their collapse is very rapid. Numerical simulations have difficulty accurately capturing these small bubbles and can only provide a macroscopic view of the cavitation process.

Based on the fundamental theory of bubble dynamics, neglecting liquid viscosity, compressibility, surface tension, and considering only the inertial effects, the Rayleigh equation describing the radial motion of a bubble wall can be obtained:

$$R_b \frac{D^2 R_b}{Dt^2} + \frac{3}{2}(\frac{DR_b}{Dt})^2 = -\frac{1}{\rho_l}(p_d(t) - p_v) \tag{1}$$

Where R_b is the radius of the bubble, ρ_l is the liquid density, $p_d(t)$ is the external driving pressure on the bubble, p_v is the saturation vapor pressure.

By taking the time derivative of the Rayleigh equation and rearranging it:

$$R_b \frac{D^3 R_b}{Dt^3} + 4\frac{DR_b}{Dt}\frac{D^2 R_b}{Dt^2} = -\frac{1}{\rho_l}\frac{\partial p_d(t)}{\partial t} \tag{2}$$

When the cavitation bubble collapses to its minimum radius, $R_b \to 0$, the term $R_b \frac{D^3 R_b}{Dt^3}$ can be neglected. Therefore, the equation can be simplified to:

$$\frac{D^2 R_b}{Dt^2} = -\frac{1}{4\rho_l \frac{DR_b}{Dt}}\frac{\partial p_d(t)}{\partial t} \tag{3}$$

From equation (3), the radial acceleration of the spherical bubble is directly proportional to the environmental pressure change rate. According to Newton's second law, force is proportional to acceleration. Therefore, the magnitude of the impact load is directly proportional to

the bubble's acceleration during rebound. Based on equation (3), it can be deduced that the impact load during cavitation bubble collapse is directly proportional to the environmental pressure change rate. When the external environmental pressure rapidly increases, the contraction acceleration of the spherical bubble also rapidly increases, leading to an accelerated collapse process and an increased likelihood of cavitation erosion risk.

Numerical results indicate that the sheet cavitation collapse is accompanied by the release of significant pressure, as shown in Figure 6(f). The collapse of sheet cavitation creates a high-pressure environmental condition for the collapse of smaller bubble. Thereby, a huge pressure which can destroy the material may be produced by the smaller bubble. However, numerical methods cannot obtain a huge pressure because of the limit of the computing resource. Therefore, the increasing pressure caused by the collapse of sheet cavitation becomes a qualitative criterion for determining the presence or absence of cavitation erosion risk. According to the characteristics of an incompressible solver, the pressure generated during the collapse of cavitation bubbles can instantaneously propagate to other locations in the flow field. Using the fluctuating pressure at the ship's bottom plate, can reflect the pressure fluctuations caused by the cavitation collapse near blades.

In conclusion, it is considered that a propeller has cavitation erosion risk when the fluctuating pressure change rate at the ship's bottom plate ($\dot{P}$) between the minimum and maximum fluctuating pressure during a single period exceeds a certain threshold C_1. The indicator for determining the presence or absence of cavitation erosion risk is:

$$\dot{P} = \frac{\Delta p}{\Delta t} = \frac{p_{\max} - p_{\min}}{t_{\max} - t_{\min}} > C_1 \tag{4}$$

2.2 Cavitation Erosion Risk Areas and Intensity determination Method

This paper simultaneously utilizes the local pressure change rate and potential energy change rate as parameters for predicting cavitation erosion risk. Both parameters reflect the severity of local bubble collapse. Regions with a significant pressure change rate, exceeding a certain threshold, are mainly found near the blade trailing edges. However, there are areas without cavitation. Regions with potential energy change rate exceeding a specific threshold correspond to areas with significant changes in vapor volume fraction. These regions are concentrated at the edge of the sheet cavitation, but sheet cavitation near the propeller blade's leading edge typically does not lead to cavitation erosion. By jointly using these two parameters to identify potential cavitation erosion risk areas is proved to be valid. After meeting the above conditions, the integral of the potential energy change rate radiating to the blade surface over a period of time is computed on the blade surface, which used to characterize the cavitation erosion risk areas and intensity.

Hammitt prompted the potential energy hypothesis (1980), which defines the potential energy of a bubble is equal to the product of the pressure difference inside and outside the bubble and the bubble's volume, as shown in equation (5). In this paper, it is assumed that for cavities that meet the screening criteria and undergo the process of collapse, the potential energy of the cavities is radiated to the wall surface without any loss.

$$E_p = (p_d(t) - p_v) \cdot V_v \tag{5}$$

Taking the time derivative of Equation (5) and dividing by the grid volume V_{cell}, yields the potential energy change rate:

$$\dot{e_{pot}} = \frac{DE_p / Dt}{V_{cell}} = (p_d(t) - p_v) \cdot \frac{D\alpha_v}{Dt} + \alpha_v \cdot \frac{\partial p_d(t)}{\partial t} \tag{6}$$

Here, α_v represents the vapor volume fraction for a single grid, and in previous studies (Melissaris, 2020), $\alpha_v \cdot \frac{\partial p_d(t)}{\partial t}$ was considered a small quantity that can be neglected. Therefore, potential energy change rate can be written as:

$$\dot{e_{pot}} = (p_d(t) - p_v) \cdot \frac{D\alpha_v}{Dt} \tag{7}$$

In this paper, cavitation collapse processes with sufficient intensity are screened by determining a threshold. The paper employs a percentage threshold method to avoid differences under different working conditions and model conditions. Therefore, the percentage threshold method for determining cavitation erosion risk areas is as follows:

It is assumed that when the instantaneous local pressure change rate exceeds 10% of the maximum pressure change rate within a certain period (multiple cavitation cycles), the impact load caused by the cavity is considered to have cavitation erosion potential. This can be expressed as follows:

$$\frac{\frac{\partial p_d(t)_i}{\partial t}}{(\frac{\partial p_d(t)}{\partial t})_{\max}} > 10\% \tag{8}$$

Where i represents a single time step.

It is assumed that when the instantaneous local potential energy change rate exceeds 10% of the maximum instantaneous potential energy change rate over a certain period (multiple cavitation cycles), the impact load caused by the cavity is considered to have cavitation erosion potential. This can be expressed as follows:

$$\frac{\dot{e}_{pot,i}}{(\dot{e}_{pot})_{\max}} > 10\% \tag{9}$$

The processes meeting both of the above parameters can be considered as having enough collapse intensity. Only these processes can be involved in the computation of cavitation erosion risk.

Because cavitation is not caused by a single impact but rather the result of multiple impacts stacking up, after identifying cavitation erosion risk area, integrating the

potential energy rate of change on the blade surface will provide the cumulative energy on the wall surface over a period of time. The magnitude of the accumulated energy on the surface determines the intensity of cavitation erosion risk.

Directly calculating the potential energy change rate may lead to numerical errors. However, in numerical simulations, the vapor volume fraction change rate $\frac{D\alpha_v}{Dt}$ can be directly calculated using the mass transfer source term from the Schneer and Sauer cavitation model:

$$\frac{D\alpha_v}{Dt} = \frac{\rho}{\rho_l \rho_v} \dot{m} \tag{10}$$

In the Schneer and Sauer cavitation model, the mass transfer source term can be expressed as:

$$\dot{m} = \frac{\rho_l \rho_v}{\rho} \frac{3\alpha_v (1-\alpha_v)}{R_b} \frac{DR_b}{Dt} \tag{11}$$

According to the Rayleigh equation, the second-order term in Equation (1) is small compared to the first-order term, and the Rayleigh equation can be simplified to:

$$\frac{DR_b}{Dt} = sign(p_d(t)_i - p_v) \sqrt{\frac{2}{3} \frac{|p_d(t)_i - p_v|}{\rho_l}} \tag{12}$$

Only calculate the potential energy rate in cavitation collapse process, In this case $p_d(t)_i > p_v$. From Equation (7), (10), (11), and (12), the potential energy rate can be induced:

$$\dot{e}_{pot,i} = (p_d(t)_i - p_v) \cdot (4\pi n)^{1/3} (3\alpha_{v_i})^{2/3} (1-\alpha_{v_i})^{4/3} \sqrt{2/3 \frac{(p_d(t)_i - p_v)}{\rho_l}} \tag{13}$$

Integrating the potential energy rate over a period of time (usually several cavitation cycles) yields the cumulative energy on the surface. The magnitude of the cumulative energy on the surface determines the intensity of cavitation erosion risk:

$$I_E = \sum_{i=1}^{n} (p_d(t)_i - p_v) \cdot (4\pi n)^{1/3} (3\alpha_{v_i})^{2/3} (1-\alpha_{v_i})^{4/3} \sqrt{2/3 \frac{(p_d(t)_i - p_v)}{\rho_l}}, \; p_d(t)_i > p_v \tag{14}$$

The complete cavitation erosion risk prediction method is as follows:

$$I_E = \sum_{i=1}^{n} (p_d(t)_i - p_v) \cdot (4\pi n)^{1/3} (3\alpha_{v_i})^{2/3} (1-\alpha_{v_i})^{4/3} \sqrt{2/3 \frac{(p_d(t)_i - p_v)}{\rho_l}} \begin{cases} p_d(t)_i > p_v \\ \dot{P} > C_1 \\ \dfrac{\frac{\partial p_d(t)}{\partial t}}{(\frac{\partial p_d(t)}{\partial t})_{\max}} > 10\% \\ \dfrac{\dot{e}_{pot}}{(\dot{e}_{pot})_{\max}} > 10\% \end{cases} \tag{15}$$

Where i represents a single time step. C_1 Will be determined in Section 4.2.

3 NUMERICAL SIMULATION METHOD

3.1 Model Introduction

Table 1 Ship model main parameters

Parameter	degree	Case1	Case2	Case3
LPP	m	7.04	7.17	7.23
BWL	m	1.25	1.31	1.30
D	m	0.397	0.452	0.46

Table 2 Propeller model main parameters

Parameter	degree	Case1	Case2	Case 3-1	Case 3-2	Case 3-3
Blade number	-	4	4	4	4	4
Diameter	m	0.23	0.228	0.25	0.25	0.25
Aspect Ratio	-	0.4	0.386	0.4	0.4	0.4
（P/D）0.7r	-	0.8461	0.7955	0.7714	0.7058	0.7605

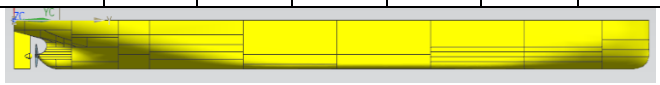

(a) Side View of the Case1 Ship Model

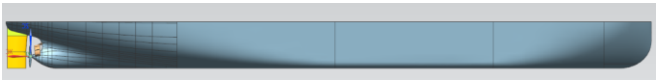

(b) Side View of the Case2 Ship Model

(c) Side View of the Case3 Ship Model

Figure 1. Ship models

(a) Case1 propeller model

(b) Case2 propeller model

(c) Case3-1 propeller model

(d) Case3-2 propeller model

(e) Case3-3 propeller model

(f) Pre-Swirl Stator model

Figure. 2. Propeller models and Pre-Swirl Stator model

Five sets of ships and propellers models were selected for unsteady cavitation flow field numerical simulations. The five sets of ship propeller models are Case1, Case2, Case3-1, Case3-2, and Case3-3. The last three sets of models use the same ship model. Case2 and Case3-3 are equipped with a Pre-Swirl Stator. The ship models and their main parameters are shown in Table 1. The propeller models and their main parameters are presented in Table 2. The three-dimensional ship model are shown in Figure 1, while the three-dimensional propeller and Pre-Swirl Stator models can be seen in Figure 2.

3.2 Computational Domain

The numerical cavitation simulations of ships and propellers are conducted in a rectangular computational domain with dimensions of length × width × height = 7Lpp × 4Lpp × 2Lpp. Boundary conditions are set as velocity inlet, pressure outlet, and the upper boundary is a symmetric plane. The other boundaries are set as no-slip walls. The computational domain and boundary settings are illustrated in Figure 3.

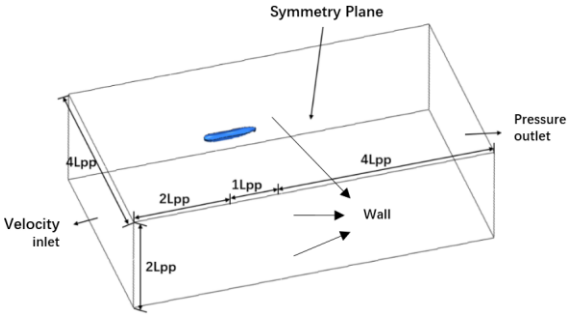

Figure 3. Computational Domain and boundary settings

3.3 Mesh Generation

This paper employs a cut hexahedral mesh throughout the entire computational domain. When approaching the ship model, the mesh is gradually refined. Given the complexity of the ship's stern, this area requires specific mesh refinement. The mesh near the ship's stern is shown in Figure 4. Further refinement is performed on the propeller surface, and a layer is added to ensure that the surface mesh satisfies $y+ \leq 1$, meeting the requirements for LES. In our previous researchs, when the mesh size between the propeller and the ship hull was less than 2mm, numerical simulations could produce fluctuating pressure time domain and frequency signals similar to experimental results. The mesh generation method for the five sets of models in this paper meets these requirements. The mesh details are presented in Table 3.

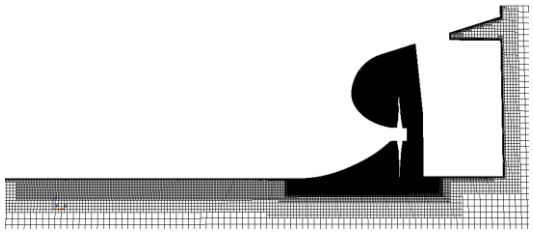

Figure 4. The mesh near the stern

Table 3. Cells number distribution

Case	Static Domain cells （millions）	Rotational Domain cells （millions）	Total cells （millions）
Case1	55.68	14.18	69.86
Case2	61.28	12.03	73.31
Case3-1	53.84	23.97	77.81
Case3-2	56.24	17.94	74.18
Case3-3	53.78	18.63	72.41

3.4 Calculation Method and Operating Conditions

The numerical simulation conditions for the 5 sets of ship propeller models are shown in Table 4.

Table 4. The numerical simulation conditions

parameter	degree	Case1	Case2	Case 3-1	Case 3-2	Case 3-3
n	rps	28	30	28	28	28
$\sigma_{n(0.8r)}$	-	0.3821	0.3424	0.2677	0.2531	0.3108
K_T	-	0.1588	0.153	0.1447	0.1374	0.1543

The environmental pressure P can be calculated:

$$\sigma_{n(0.8r)} = \frac{P - P_v}{0.5\rho(0.8n\pi D)^2} \tag{16}$$

Where P is the ambient pressure, P_v is the saturated vapor pressure, with a selected value of 3170 Pa, ρ is the liquid density, selected as 998.2 kg/m^3, D is the propeller diameter, and n is the propeller rotational speed.

The thrust coefficient can be calculated:

$$K_T = \frac{T}{\rho n^2 D^4} \tag{17}$$

Where T is the propeller thrust.

The numerical simulation determines the inlet flow velocity using the constant thrust method. The numerical calculation method begins with steady-state flow field simulations using the SST k-ω turbulence model. The steady-state results serve as the initial conditions for the transient simulations. Transient simulations employ the large eddy simulation (LES) method with a time step set to one-degree rotation of the propeller per step. After two full rotations of the propeller in the transient simulation, the Schneer and Sauer cavitation model is activated, and the calculation ends after an additional two rotations of the propeller.

4 NUMERICAL PREDICTION RESULTS OF CAVITATION EROSION RISK

4.1 Analysis of Cavitation Patterns

Numerical prediction of cavitation erosion risk first requires ensuring the accuracy of the cavitation flow field. In this paper, the cavitation numerical results of 5 sets of ships and propellers are compared with the cavitation results from model experiments, as shown in Figure 5 to 9.

From Figure 5, it can be observed that for Case1, the cavity volume gradually increases from 0° to 30° of propeller rotation, decreases from 30° to 50° of propeller rotation. The numerical results match well with the experimental results. A high-pressure area appears on the lower right corner of the sheet cavitation on the blade surface. However, its distribution is more scattered, and the amplitude is not as pronounced as in other areas.

From Figure 6, it can be seen that for Case2, the cavity volume gradually increases from 0° to 40° of propeller rotation, decreases from 40° to 50° of propeller rotation.

At 50° propeller rotation, the sheet cavitation appears with a concave structure at the trailing edge, and at the lower right corner of the blade surface, there is a significantly higher pressure area than in other regions.

From Figure 7, it can be observed that for Case3-1, the cavity volume gradually increases from 0° to 30° of propeller rotation and decreases from 30° to 60° of propeller rotation. During the period from 45° to 50° of propeller rotation, the sheet cavitation is cut in the middle, splitting into two cavitation structures, with high-pressure areas appearing downstream of both cavitation structures. The numerical results match well with the experimental results.

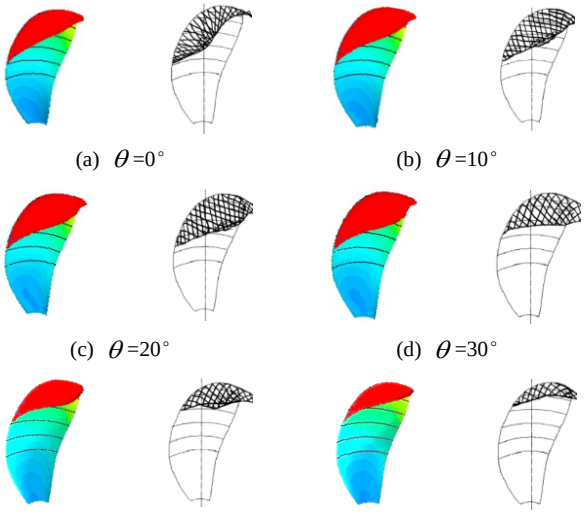

(a) θ=0° (b) θ=10° (c) θ=20° (d) θ=30° (e) θ=40° (f) θ=50°

Figures 5. Comparison of Unsteady Cavitation Numerical Results with Experimental Results for Case1

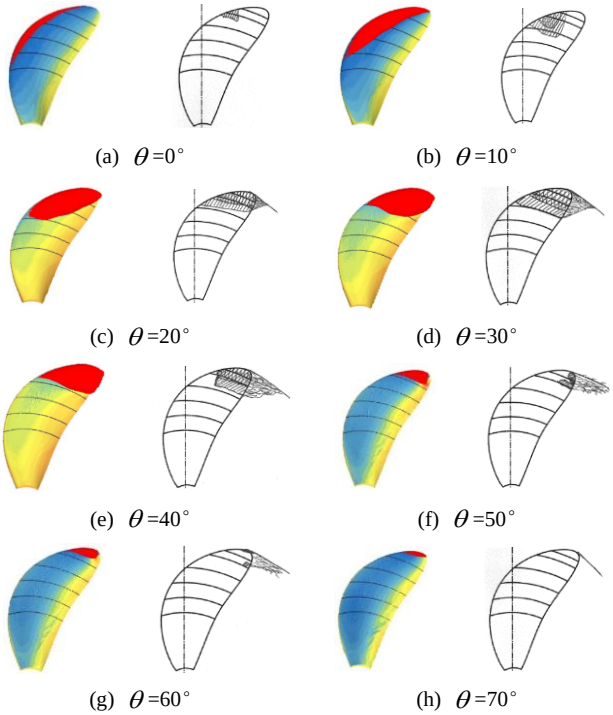

(a) θ=0° (b) θ=10° (c) θ=20° (d) θ=30° (e) θ=40° (f) θ=50° (g) θ=60° (h) θ=70°

Figures 6. Comparison of Unsteady Cavitation Numerical Results with Experimental Results for Case2.

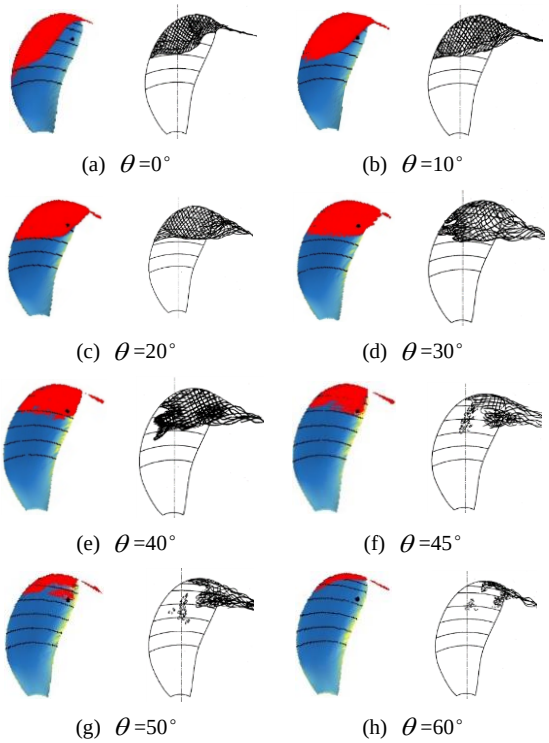

(a) θ=0° (b) θ=10° (c) θ=20° (d) θ=30° (e) θ=40° (f) θ=45° (g) θ=50° (h) θ=60°

Figures 7. Comparison of Unsteady Cavitation Numerical Results with Experimental Results for Case3-1

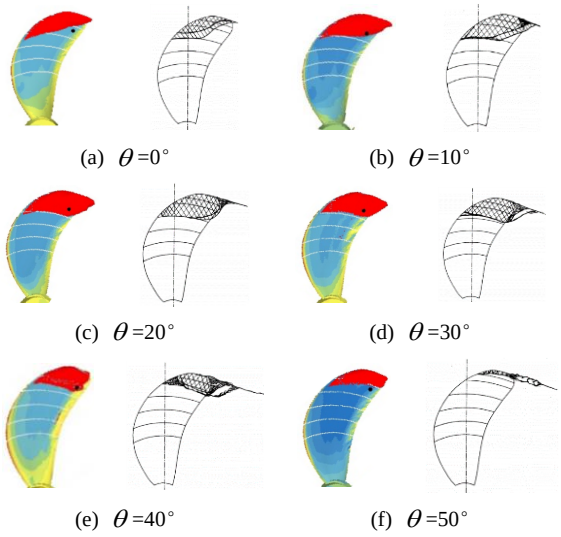

(a) θ=0° (b) θ=10° (c) θ=20° (d) θ=30° (e) θ=40° (f) θ=50°

Figures 8. Comparison of Unsteady Cavitation Numerical Results with Experimental Results for Case3-2

From Figure 8, it can be seen that for Case3-2, the bubble volume gradually increases from 0° to 30° and decreases from 30° to 50° of propeller rotation. The numerical results match well with the experimental results. At 40° propeller rotation, a concave structure appears on the trailing edge of the sheet cavitation, with significantly higher pressure around the concave structure.

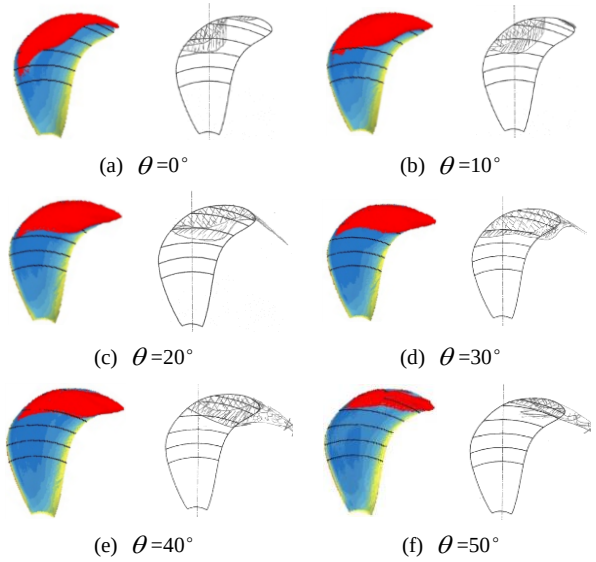

Figures 9. Comparison of Unsteady Cavitation Numerical Results with Experimental Results for Case3-3

From Figure 9, it can be observed that for Case3-3, the cavity volume gradually increases from 0° to 30° of propeller rotation and decreases from 30° to 50°of propeller rotation. The numerical results match well with the experimental results. There is no significant high-pressure area at the trailing edge of the sheet cavitation.

Based on the characteristics of the cavitation pattern numerical results, when there is cavitation splitting or the appearance of concave structures in cavitation patterns, it is accompanied by the emergence of local high-pressure areas and a rapid decrease in cavitation volume. This phenomenon is closely related to the formation of cavitation erosion risk. The regular growth and reduction of cavities does not cause significant pressure changes on the blade surface, and therefore, it does not create conditions for cavitation erosion risk.

4.2 Results and Analysis of Fluctuating Pressure on the Ship's Bottom Plate

This study previously investigated the independence of mesh and time step of the numerical calculation of fluctuating pressure on the ship's bottom plate, and it was found that when the mesh size between the rotating domain and the ship's bottom plate is less than 2mm, for most ship propeller models, similar time-frequency characteristics to experimental results can be obtained. When the time step is set to one degree of propeller rotation (approximately 1×10^{-4}s), the amplitude of fluctuating pressure is relatively close to the experimental results.

During the unsteady cavitation calculations, fluctuating pressure at the ship's bottom plate was simultaneously monitored. The location of the fluctuating pressure monitoring points are indicated by the red dots in Figure 10, which corresponds to the same location as in the experimental measurements.

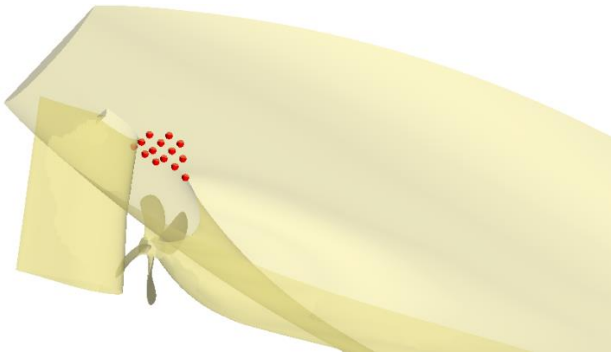

Figure 10. fluctuating pressure monitoring points

Case2 propeller is selected to analyze the variation characteristics of fluctuating pressure within one period, as shown in Figure 11. From the figure, it can be observed that the fluctuating pressure gradually increases from 30° to 50°, corresponding to the cavitation pattern in Figure 6, which is the gradual reduction of sheet cavitation. At 50° propeller rotation, the fluctuating pressure reaches its peak, coinciding with the moment when a high-pressure area appears in the lower right corner of the sheet cavitation. Therefore, it can be observed that the process from the lowest point to the highest point of fluctuating pressure within the red box area in Figure 11 coincides with the cavitation collapse stage. The fluctuating pressure change rate can effectively display the intensity of the environmental pressure field changes, thereby qualitatively reflecting the strength of cavitation collapse. From multiple fluctuating pressure cycles in Case2, the maximum fluctuating pressure change rate is calculated according to Equation (4): $\dot{P}=1.375\times10^{6}$ pa • s^{-1}.

Figure 12 shows the numerical simulation results of time-domain signals of fluctuating pressure at the ship's bottom plate for the five cases. Table 5 presents the maximum fluctuating pressure change rate and the experimental cavitation erosion risk results. It was observed that there is a significant difference in the maximum fluctuating pressure change rate between cases with cavitation erosion risk and cases without cavitation erosion risk in the experimental results. In this study, a preliminary threshold for cavitation erosion risk is established as the maximum fluctuating pressure change rate exceeding $C_1=1.2\times10^{6}$ pa • s^{-1}. This threshold is derived from the five ship propeller cases in this paper and can be further optimized based on additional cases in the future.

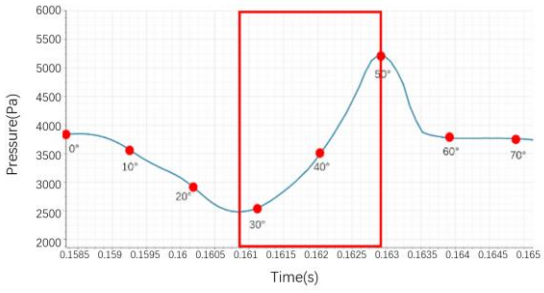

Figure 11. Distribution of fluctuating pressure at different angles within one cavitation period for Case2

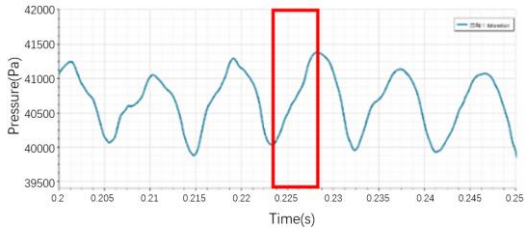

(a) Time-domain signal of fluctuating pressure for Case1

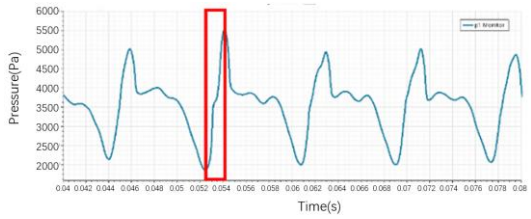

(b) Time-domain signal of fluctuating pressure for Case2

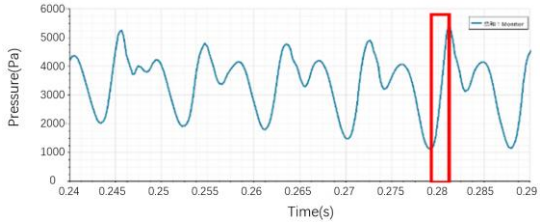

(c) Time-domain signal of fluctuating pressure for Case3-1

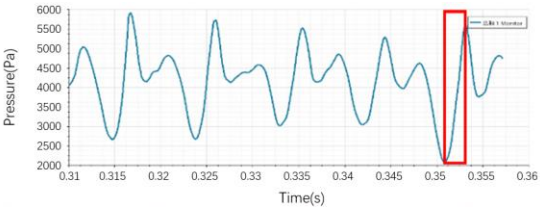

(d) Time-domain signal of fluctuating pressure for Case3-2

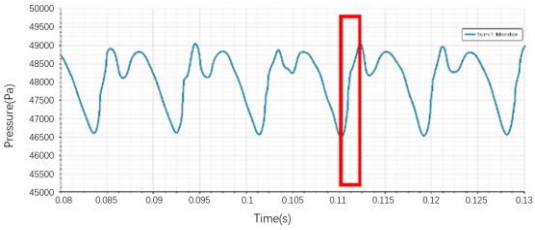

(e) Time-domain signal of fluctuating pressure for Case3-3

Figure 12. Time-domain signal of fluctuating pressure for the five cases

Table 5. fluctuating pressure change rate and cavitation erosion risk results for five cases

Case	the maximum fluctuating pressure change rate （pa • s^{-1}）	experimental cavitation erosion risk results
Case1	2.8×10^5	No
Case2	1.8×10^6	Yes
Case3-1	2.3×10^6	Yes
Case3-2	1.5×10^6	Yes
Case3-3	9.6×10^5	No

4.3 Numerical Prediction Results of Cavitation Erosion Risk

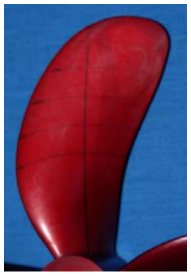

(a) Comparison between numerical cavitation erosion risk results and experimental results for Case1

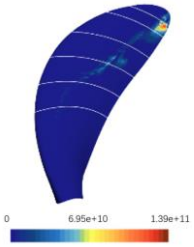

(b) Comparison between numerical cavitation erosion risk results and experimental results for Case2

(c) Comparison between numerical cavitation erosion risk results and experimental results for Case3-1

(d) Comparison between numerical cavitation erosion risk results and experimental results for Case3-2

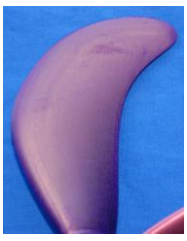

(e) Comparison between numerical cavitation erosion risk results and experimental results for Case3-3

Figure 13. The cavitation erosion risk prediction results for the five aft ship propeller cases

Figure 13 displays the cavitation erosion risk prediction results for the five aft ship propeller cases. Among these

cases, Case1 and Case3-3 did not exhibit cavitation erosion risk. Cavitation erosion areas of Case2 occur approximately at 0.95r along the trailing edge. The numerical prediction results in this paper match the actual ship cavitation erosion results, validating the applicability of this cavitation erosion risk prediction method to actual ships. In the experiments for Case3-1 and Case3-2 models, cavitation erosion risk was observed, with both propeller cases showing cavitation erosion risk locations between 0.8r and 0.95r. Case3-1 had more severe results, and the cavitation erosion risk numerical prediction method presented in this paper matches well with the experimental results. In conclusion, the cavitation erosion risk prediction method in this paper demonstrates good practical applicability in engineering.

5 CONCLUSION

Based on the cavitation mechanism and numerical simulation characteristics, this paper proposes a numerical prediction method for cavitation erosion risk assessment in aft ship propellers. This method involves assessing the existence of cavitation erosion risk by determining whether the rate of change of fluctuating pressure at the ship's bottom plate between its minimum and maximum fluctuating pressure within a single cycle exceeds a certain threshold. Furthermore, it filters out the features with cavitation erosion potential by evaluating the pressure change rate on the blade surface, which exceeds 10% of the maximum pressure change rate over a period (multiple cavitation cycles), and the potential energy change rate on the blade surface, which exceeds 10% of the maximum potential energy change rate over a certain period. The integrated potential energy change rate on the blade surface that meets the criteria over a specific period (multiple cavitation cycles) provides the distribution and intensity of cavitation erosion risk. The main conclusions obtained are as follows:

(1) Based on the comparison between the fluctuating pressure amplitude at the ship's bottom plate and the experimental cavitation erosion risk results for the 5 aft ship propeller cases, it was observed that the cases with cavitation erosion risk exhibited significantly higher fluctuating pressure change rates between the minimum and maximum fluctuating pressure during a single cycle compared to cases without cavitation erosion risk. In this paper, a fluctuating pressure change rate greater than 1.2×10^6 is adopted as the criterion for determining the presence of cavitation erosion risk.

(2) In the five selected cases of aft ship propellers in this paper, three of them exhibited cavitation erosion risk in experimental or practical propellers. A comparison between the numerical cavitation erosion risk results and the experimental and practical ship results revealed a good agreement in terms of the distribution and intensity of cavitation erosion risk. This validation confirms the practical applicability of the cavitation erosion risk prediction method proposed in this paper.

REFERENCES

Pan S S, Peng X X. (2013). Cavitation Mechanism. National Defence Industry Press. China.

Cao Y T (2017) ‘A Qualitative Study on the Relationship Between Cavitation Structure and Erosion Region around a 3D Twisted Hydrofoil by Painting Method’. Fifth International Symposium on Marine Propulsors.

Li Z R. (2012). ‘Assessment of Cavitation Erosion with a Multiphase Reynolds-Averaged Navier-Stokes Method’.

Dular M. (2006). ‘Experimental and Numerical Modeling of Cavitation Erosion’. Cav2006,

Ikohagi T, Iga Y , Nohmi M. (2008). ‘Numerical Prediction Method of Cavitation Erosion’ Asme Fluids Engineering Division Summer Meeting Collocated with the Heat Transfer.

Leclercq C (2016). ‘Numerical investigations on cavitation intensity for 3D homogeneous unsteady viscous flows’. Iop Conference.

Archer A, Flageul C, Patella R F. (2012). ‘Numerical and experimental investigations on cavitation erosion’. The 26th IAHR Symposium on Hydraulic Machinery and Systems.

Bulten N, Melissaris T, Schenke S. (2020). ‘On the accuracy of predicting cavitation impact loads on marine propellers’. Wear.

Hammitt F G.(1980). ‘Cavitation and multiphases flow phenomena’. McGraw-Hill.